# Can Automated Vehicles "See" in Minnesota? Ambient Particle Effects on LiDAR

**William Northrop, Principal Investigator**
Department of Mechanical Engineering

**AUGUST 2022**

Research Report
Final Report 2022-03

## Technical Report Documentation Page

| 1. Report No.<br>MN 2022-03 | 2. | 3. Recipients Accession No. | |
|---|---|---|---|
| 4. Title and Subtitle<br>Can Automated Vehicles "See" in Minnesota? Ambient Particle Effects on LiDAR | | 5. Report Date<br>August 2022 | |
| | | 6. | |
| 7. Author(s)<br>William Northrop, Lu Zhan, Shawn Haag, Darrick Zarling | | 8. Performing Organization Report No. | |
| 9. Performing Organization Name and Address<br>Mechanical Engineering Department<br>University of Minnesota<br>Mechanical Engineering Building, 111 Church St SE<br>Minneapolis, MN 55455 | | 10. Project/Task/Work Unit No.<br>CTS #2020028 | |
| | | 11. Contract (C) or Grant (G) No.<br>(c) 1035427 | |
| 12. Sponsoring Organization Name and Address<br>Minnesota Department of Transportation<br>Office of Research & Innovation<br>395 John Ireland Boulevard, MS 330<br>St. Paul, Minnesota 55155-1899 | | 13. Type of Report and Period Covered<br>Final Report: February 2020-August 2022 | |
| | | 14. Sponsoring Agency Code | |
| 15. Supplementary Notes<br>https://www.mndot.gov/research/reports/2022/202203.pdf | | | |
| 16. Abstract (Limit: 250 words)<br>This project will use a combination of laboratory experimentation and road demonstrations to better understand the reduction of LiDAR signal and object detection capability under adverse weather conditions found in Minnesota. It will also lead to concepts to improve LiDAR systems to adapt to such conditions through better signal processing image recognition software. | | | |
| 17. Document Analysis/Descriptors<br>Fog, Snowfall, Laser radar, Automated vehicles | | 18. Availability Statement<br>No restrictions. Document available from:<br>National Technical Information Services,<br>Alexandria, Virginia  22312 | |
| 19. Security Class (this report)<br>Unclassified | 20. Security Class (this page)<br>Unclassified | 21. No. of Pages<br>36 | 22. Price |

# Can Automated Vehicles "See" in Minnesota? Ambient Particle Effects on LiDAR

## FINAL REPORT

*Prepared by:*

William Northrop
Lu Zhan
Shawn Haag
Darrick Zarling
Department of Mechanical Engineering
University of Minnesota

## August 2022

## ACKNOWLEDGMENTS

# TABLE OF CONTENTS

# EXECUTIVE SUMMARY

**Research Issue:**

To achieve full automation in self-driving vehicles, environmental perception sensing accuracy is critically important. However, ambient particles in adverse weather like foggy, rainy, or snowy conditions can significantly scatter the incident laser beam, and therefore contaminate the intensity and accuracy of light detection and ranging (LiDAR) sensors. Especially compared to the rapidity of technology development in self-driving vehicles, there is a significant lack of documented research on LiDAR systems with wavelengths longer than 1 $\mu m$ for application in Advanced Driver-Assistance Systems. This project team at the University of Minnesota takes on that challenge in partnership with a forward-thinking LiDAR company that understands the importance of ensuring that automated vehicles (AVs) must navigate in all weather and a Minnesota AV research organization.

**Results:**

A fog chamber experiment was performed with a state-of-the-art 1.55 $\mu m$ wavelength automotive-grade LiDAR system in a controlled laboratory fog chamber. The goal of the research was to correlate laser attenuation and the optical properties of fog particles. In this work, a thorough multistep procedure for LiDAR data analysis was presented including spatial averaging of the object measurement and characterizing the temperature effect on a LiDAR intensity parameter. Fog particle density was measured by a commercial visibility sensor instrument. Assuming a constant extinction coefficient and backscatter coefficient, a simple analytical model was derived that correlates LiDAR reflectance and extinction coefficient measured by visibility sensor. Results showed that the correlation coefficient between LiDAR and visibility sensor data was 0.98 and the R-squared value of linear fitting was 0.96. By comparing the LiDAR original signal and the model, the Root-Mean-Squared Deviation was 0.007, meaning the model performed very well for predicting LiDAR reflectance in the controlled environment. Furthermore, although the returned signal strength was attenuated, the LiDAR can measure the target with a visibility range lower than six meters and the accuracy is within 5 cm.

Unlike fog particles, snow particles were generally larger and therefore reflected a larger portion of laser energy. According to this feature, we adopted a different data-processing strategy, which Instead of characterizing the laser attenuation, a snow filter was developed based on the cut-off reflectance value calculated from first principle. A visualization of the result was presented in Figure 11. However, if the precipitation of snow becomes serious, the laser lens may be blocked by a thick layer of ices and lose 99% of the data due to this blockage effect. This is very crucial as such a huge loss of real-time data can cause tremendous safety issues during a severe snow event. Better design in the hardware level such as installing the LiDAR internally or adding a heat unit around the lens may alleviate the blockage effect from ice.

**Recommendations:**

By combining the data from the two experiments, we can conclude that:

1. A mathematical correlation was derived and validated by the data of the fog experiment. The model was used to predict LiDAR performance or visibility under fog conditions. Moreover, this methodology can be extended to different scenarios where homogenous ambient particles are expected.
2. LiDAR data was mainly corrupted due to the ice accumulation on the LiDAR lens. Improvement will be required at the hardware level to palliate such blockage effects.
3. A snow particle filter was designed and tested with the LiDAR data and showed the most significant potential to remove the outliers due to adverse weather. Applying such a filter can be beneficial in the data post-processing and algorithm improvement analysis.

MnDOT could consider agricultural dust, due to Minnesota's grain harvest season, and other non-water particles in future LiDAR-related projects. Due to the focus of our research on fog and snow particles, the research team will be unable to pursue any specific research on dust particles. Public safety knowledge related to LiDAR to guide policy and regulation is also not considered as this was not part of the original objectives of this research. The research team suggests future research may be required to further assess policy implications of LiDAR and connected and automated vehicle (CAV) technologies.

**Benefactors:**

The completed work mainly addresses the issue of advancing CAV technology in winter conditions, a stated MnDOT CAV-X Office goal. By better understanding the impact of particles like snow and mist, practitioners can develop better object recognition capabilities for winter environments. Minnesota roads provide an ideal testing ground for winter AV testing. Through on-road experiments, the project accelerates the development of real-world LiDAR technology in Minnesota and globally.

This project used a combination of laboratory experiments and road demonstrations to understand the reduction of LiDAR signal and object detection capability under adverse weather conditions found in Minnesota. It also led to new concepts to improve LiDAR systems to adapt to such conditions through better signal processing image recognition software.

In the short term, the work will advance CAV policy in Minnesota by providing crucial information about what weather conditions are appropriate for on-road testing and the development of new AVs. While advancing AV technology is essential, maintaining proper safety margins on navigation systems are required for any vehicles on Minnesota roads. Longer-term, the project results can lead or contribute to stronger state safety regulations for AVs. Other measures of success include the use of data and correlations produced in the project by LiDAR manufacturers, system integrators, and vehicle manufacturers. Incorporating developed correlations into AV products, either directly into image processing software or hardware or software changes during the design process, will be critical indicators that show the project successfully impacts the field.

# CHAPTER 1: LITERATURE REVIEW

## 1.1 INTRODUCTION

Since the 1960s, Light Detection and Ranging (LiDAR) technology has been well-established in both academia and industry. LiDAR is a surveying method that measures distance to a target by illuminating the target with laser light and measuring the reflected light with a sensor. Methods include time of flight (ToF), Doppler frequency shift or polarization. Regarding autonomous vehicles, this literature review is focused on ToF imaging LiDAR, which specifically measures the distance between the apparatus and hard targets. From the first lasers ranging to the moon achieved in 1969 [1] to the first commercial LiDAR system installed on autonomous vehicles in 2005 [2], the ToF LiDAR technique has made great strides historically and provides a significant role in the application of autonomous vehicles.

The use of LiDAR in the automated vehicle (AV) industry is a relatively novel use of the technology, though it is considered an essential component of AV navigation systems. The laser technique improves the versatility and efficiency of mobile robots by directly mapping static environments and identifying moving objects nearby. Notwithstanding a suite of sensors (radar, optical camera, and ultrasound), LiDAR complements the environmental detection in terms of long-range and high resolution. To achieve the full automation level, which refers to the complete automatic control of a vehicle under all conditions [3], an accurate environmental perception is always required, even under adverse weather such as haze, snow, rain, or fog.

However, even the most state-of-art automotive sensor systems experience non-negligible attenuation in data quality due to adverse weather [4]. Subjected to the interaction of aerosol particles with light, the LiDAR system provides sensitive and instantaneous responses to such unfavorable atmospheric conditions, where the degradation in signal is normally presented. This is beneficial in atmospheric research as many aerosol properties are measured, like particle size and concentration [5]. It is nonetheless a hurdle, to overcome in autonomous vehicle applications as the maximum (or average) range detected may be reduced.

It is, therefore, of importance to characterize the impact of aerosol properties on LiDAR measurement, via which more advanced processing algorithms can be developed for correction, calibration, and prediction. Moreover, such study will potentially benefit new hardware design to tackle the challenge of the extreme environment [6].

The chapter is organized as follows: Key aspects of the LiDAR system are described in section 1.2. LiDAR research on aerosol properties in the atmosphere is reviewed in section 1.3. Finally, in section 1.4, the up-to-date investigation of particle effects on the automated LiDAR system is summarized. Section 1.5 provides concluding remarks.

## 1.2 LIDAR SYSTEM

As stated in the introduction, LiDAR includes a wide range of phenomenology, thus many standards for categorization. There is a focus on the pulsed imaging LiDAR that is commonly used in aerosol particle research and automated vehicle perception. Some key aspects of the LiDAR system are reviewed, such as laser wavelength, pulse energy, scanning mode and range resolution, while the LiDAR range equation is given along with the explanation. The range equation forms the framework of approaches in aerosol particle research.

By definition, a LiDAR instrument uses the electromagnetic waves in the visible and infrared spectrum (wavelengths approximately from $10^{-5}$ m to $10^{-6}$ m), which fundamentally differentiates itself from X-band radar (typically wavelength of 3 cm) and L-band radar (wavelength of 30 cm). LiDAR systems can be equipped with a laser at an ultraviolet wavelength [7] or lasers at multi-wavelengths [8], the review of which is beyond the scope of this report. Numerous factors can influence the design of laser wavelengths, one of which is the Shannon sampling theorem. The theorem states that the instrument must utilize a sampling interval no greater than half-size of the resolvable feature of the study object, for instance, the size of aerosol particle. In other words, if the laser wavelength is significantly larger than the size of particles, it just flows around them with less or no attenuation. For a typical 1500 nm wavelength, the LiDAR technique is more capable in measuring properties of tiny particles in the atmosphere than radar techniques, however, the LiDAR technique is less powerful in penetrating the rain droplets, fog or dust for long-range measurement. Another factor to consider is the laser safety category as a stronger laser power may damage a human retina. In general, people assume 10 seconds of eye exposure to calculate the total absorbed pulse energy when categorizing laser safety. Given that the surface of a human eye has varied absorptivity as to laser wavelength, the maximum permissible laser flux is at the wavelength around 1500 nm [9]. The laser device used in AV applications is therefore normally less than 1500 nm due to the restriction of laser safety class 1. The maximum allowed power for 1500 nm laser is less than 100 mW.

Another key aspect of imaging LiDAR is the angular resolution. Unlike 3D flash LiDAR, which uses a large array of detectors to develop images, commercial scanning LiDAR has a single detector or a limited number of individual detectors and high-speed scanners to direct the lasers. Consequently, the angular resolution is determined by the rotation speed of the scanner and sampling frequency of the system. The 3D imaging LiDAR currently available for autonomous vehicles in the market is pushing the resolution high enough to recognize a paper bag from a child on the street. The range resolution of LiDAR can be defined as the minimum distance to separate two independent measurement points, and can be determined by the equation as follows [9]:

$$\Delta R = \frac{c}{2B}$$

Where c is the speed of light in a specific medium, and B indicates the bandwidth of the returned signal. For a commercial LiDAR system on autonomous vehicles, the range resolution can be as accurate as 0.3 cm. Furthermore, if the range to an object is sufficiently long enough such that the system is 'confused'

with the return signal from the next signal, Eq. 1 can then define the maximum range without ambiguity. This can be done by simply replacing the bandwidth, B, with the pulse repetition frequency (PRF).

The returned LiDAR signal can be written in the simplest form as [10]:

$$P(R, \lambda) = KG(R)\beta(R, \lambda)T(R, \lambda)$$

Note the power P received from a distance R is determined by four factors. The first factor, K, summarizes the performance of the LiDAR system, the second, $G(R)$, describes the range-dependent measurement geometry. These two factors are completely determined by the LiDAR setup and can thus be controlled by the experimentalist. The information on the atmosphere, and thus all the measurable quantities, are contained in the last two factors of above equation. The term $\beta(R, \lambda)$ is the backscatter coefficient at distance R. It stands for the ability of the atmosphere to scatter light back into the direction from which it comes. $T(R, \lambda)$ is the transmission term and describes how much light gets lost on the way from the LiDAR to distance R and back. Both $\beta(R, \lambda)$ and $T(R, \lambda)$ are the subjects of investigation and, in principle, unknown to the experimentalist.

Considering the LiDAR academic research on atmospheric aerosol particles and the practical goal in this project, we herein focus on elaborating the $\beta(R, \lambda)$ and $T(R, \lambda)$. In the atmosphere, the laser light is scattered by air molecules and particulate matter. i.e., $\beta(R, \lambda)$ can be written as:

$$\beta(R, \lambda) = \beta_{mol}(R, \lambda) + \beta_{aer}(R, \lambda)$$

This dual effect can be modeled individually, however, is difficult to separate from the pulse imaging LiDAR measurement. There are two main regimes of scattering based on the comparison in size between particles and laser wavelength. Rayleigh scattering is the in-all-direction elastic scattering of light by molecules and particulate matter that are much smaller than the wavelength of the incident light. The scattering intensity is proportional to the sixth power of the diameter of the particles and inversely proportional to the fourth power of the wavelength of light [9]. Mie scattering is the second type of mechanism where particles are on the order of the same size as the laser wavelength or much larger. Particles with Mie scattering have mostly forward scattering. As the final part of the LiDAR equation, we have to consider the fraction of light that gets lost on the way from the LiDAR to the scattering volume and back. The transmission term $T(R, \lambda)$ can take values between 0 and 1 and is given by

$$T(R, \lambda) = exp\left[-2\int_0^R \alpha(r, \lambda)dr\right]$$

This term results from the specific form of the Lambert–Beer–Bouguer law for LiDAR. The integral considers the path from the LiDAR to distance R. The sum of all transmission losses is called light extinction, and $\alpha(r, \lambda)$ is the extinction coefficient. Similar to the backscatter coefficient, extinction can occur because of scattering and absorption of light by molecules and particles. It, therefore, can be written as the sum of four components:

$$\alpha(r, \lambda) = \alpha_{mol,sca}(r, \lambda) + \alpha_{mol,abs}(r, \lambda) + \alpha_{aer,sca}(r, \lambda) + \alpha_{aer,abs}(r, \lambda)$$

After obtaining these optical parameters, analytical methods will be adopted to bridge the gap between LiDAR measurements and microphysical parameters of the atmospheric particles [11].

## 1.3 LIDAR SENSING OF AEROSOLS

The fundamental equations of imaging LiDAR were presented in section 2. Normally, molecular absorption is ignored [11]. There are, therefore, four unknowns in principle, namely $\beta_{mol}(R, \lambda)$, $\beta_{aer}(R, \lambda)$, $\alpha_{sac}(R, \lambda)$ and $\alpha_{aer}(R, \lambda)$, while one quantity is measured. To proceed with the solution, assumptions or more equations should be added. For instance, molecular scatters light by varying the intensity inversely proportional to the fourth power of the wavelength of light (Rayleigh scattering). Given a laser wavelength, molecular scattering changes directly with molecular number density, which is thus theoretically determined from the Rayleigh scattering law and knowledge of the atmospheric temperature and pressure profiles over the observation site [23][24][25]. By doing so, the remaining terms are the aerosol terms $\beta_{aer}(R, \lambda)$ and $\alpha_{aer}(R, \lambda)$. However, this still leaves two unknowns and only one measurement at each radial distance R. Various solution methods have been developed over the years to overcome this dilemma [26][27][28][29][30][31][32].

Many examples and details can be found in the literature. To retrieve the aerosol properties, the LiDAR equation (Eq. 2) was solved in many ways. However, the challenge is still obvious, that is, the particle backscatter coefficient and extinction coefficient, must be determined from only one measured quantity, the elastic LiDAR return. Moreover, the assumptions behind the solution are the major source of uncertainty and errors. Therefore, new laser techniques have been developed to tackle this challenge, namely Raman LiDAR and High Spectral resolution LiDAR (HSRL), which rely on multi-wavelength measurements and spectral distribution of light [33].

## 1.4 LIDAR APPLICATION ON AUTONOMOUS VEHICLES (AV)

The first benchmark of the LiDAR sensor experimental study was already performed in 1991 by Hebert and Krothov [34]. Afterwards, Pascoal et al. performed the first assessment of four different laser range finders (Sick LMS200, Hokuyo URG- 04LX, IFM Efector O1D100 and Sick DT60) and found the IFM Efector O1D100 and the Sick DT60 have the best performance [35]. Prior, Wong et al. extended this into a benchmark study where a total of 10 different range sensors were evaluated to reflect the optimality for void modeling at a critical distance [36]. In general, automotive LiDAR system experiments can be categorized into two types, one of which involves field tests with atmospheric aerosols and particles, while the other one uses controllable and detectable artificial aerosols within the atmospheric chamber for the test. One example including both types of automotive LiDAR system experiments, can be found in [37]. Trickey et al. investigated the penetration performance of the Opal LiDAR in dust, fog, snow whiteouts and smoke. Dust and fog performances have been evaluated in an aerosol chamber while snow conditions and smoke were obtained in the field tests. Two types of experiments are reviewed as follows:

- Field experiments: In [38], Peynot et al. did the initial work in collecting a large, accurately calibrated and synchronized data-set, where the common perceptual failures are identified and new methods are proposed to alleviate the corresponding errors. For laser radar systems, Rasshofer et al. theoretically investigated the influence of atmospheric parameters based on Mie's theory in order to develop a novel electro-optical laser radar target simulator system. However, their experimental accuracy was limited by the lack of calibration and scaling on the signal modeling [39]. Recently, Hasirlioglu et al. studied the disturbances due to low ambient temperatures and exhaust gases from leading vehicles [40]. A practical statement is given that the degradation of a laser signal becomes more serious with the lower temperature of exhausted gas. Kutila et al. evaluates the maximum and average detection range of a commercial LiDAR system under foggy and rainy weather. The result shows a noticeable decrement in the average range, while the maximum range is changed minimally [41].
- Fog chamber experiments: In [42], Ijaz et al. built a very small laboratory with a controlled atmospheric chamber and was able to show that the attenuation due to fog and smoke in a free space optical communication link is not wavelength dependent for visibility less than 500m and wavelengths between 600-1550 nm. A linear correlation was found between laser attenuation due to smoke particles and visibility. In the same experimental condition, they later conducted experiments and proposed a new empirical model to predict the attenuation, which outperformed the Kim and Kruse model [43]. Knowing that the laser wavelength plays a significant role in responding to atmospheric particles, a very detailed inspection and discussion of two popular wavelengths for LiDAR systems, i.e. 905 nm and 1550 nm, was completed by Wojtanowski et al. [44]. It is interesting to point out that the climate chamber of CEREMA in Clermont Ferrand (France) is the only one in Europe that is able to produce stable fog with a certain meteorological visual range V in two different fog droplet distributions, i.e. radiation fog (small droplets) and advection fog (large droplets) [45].

Unlike the atmospheric particle experiments, researchers and engineers working in the autonomous vehicle industry prefer more practical parameters rather than the aerosol optical properties. For instance, $T(R, \lambda)$ and $\alpha(R, \lambda)$ in Eq. 4 are physical parameters that are difficult to represent in road transport or the application of visibility [45]. The question has been asked: what's the meaning of fog with a transmission factor of 0.3, or with an extinction coefficient of 0.1? It is thus easier to grasp the idea of fog expressively by a visibility distance such as 30 or 100 m. On the other hand, the meteorological visibility V (km) can be linked to atmospheric attenuation coefficient and laser wavelength via the empirical model, the Kruse model [46]:

$$V = \frac{10 \log_{10} T_{th}}{\alpha(R, \lambda)} \left(\frac{\lambda}{\lambda_0}\right)^{-q}$$

$$q = \begin{cases} 1.6, & V > 50 \ km \\ 1.3, & 6 \ km < V < 50 \ km \\ -0.583 V^{\frac{1}{3}}, & V < 6 \ km \end{cases}$$

where $T_{th}$ is the visual threshold (normally is taken as 2% to 5% depends on the experimental condition). $\lambda_0$ is the maximum spectrum of the solar band. q is the adjustable parameter related to the particle size distribution in the atmosphere. Modified values of q were introduced by Kim [47], who puts effort in researching the visibility lower than 500 m,

$$q = \begin{cases} 1.6, & V > 50 \ km \\ 1.3, & 6 \ km < V < 50 \ km \\ 16V + 0.34, & 1 \ km < \ V < 6 \ km \\ V - 0.5, & 0.5 \ km < \ V < 1 \ km \\ 0, & V < 0.5 \ km \end{cases}$$

However, this model does not provide a good agreement with several recent experimental data [43][48][49][50][51]. Naboulsi has proposed a new fine-tuned correlation for advection fog $(4 - 20 \ \mu m)$ and radiation fog $(1 - 5 \ \mu m)$ in [48], and can be expressed as:

$$V = \frac{0.11478\lambda + 3.8367}{\alpha_{adv}(R, \lambda)}$$

$$V = \frac{0.18126\lambda^2 + 0.13709\lambda + 3.8367}{\alpha_{rad}(R, \lambda)}$$

Smoke and fog particles are characterized in an atmospheric chamber by Ijaz et al [43]. Results are valid for the laser wavelength within a range [550, 1550] nm, and up to 1 km visibility, which can be formulated as:

$$q = \begin{cases} 0.1428\lambda - 0.0947, & fog \\ 0.8467\lambda - 0.5212, & smoke \end{cases}$$

Using characteristics from both Ijaz and Naboulsi's results, Mustafa has developed another custom model for visibility less than 0.5 km. The expression is given as follow [52]:

$$q = \begin{cases} 0.6701 - 0.5182, & fog \\ -0.1619\lambda - 1.336, & smoke \end{cases}$$

Estimating visibility is the key step to quantify the adverse environment, which then allows one to evaluate the correlation between environmental parameters and sensor performance. Normally, the LiDAR system performance is evaluated by variables such as maximum range, averaged range, number of points, SNR or raw data intensity and associated variation [6]. The correlation above is not simply linear in general and is of great importance because the most state-of-the-art detection algorithms are based on undisturbed LiDAR data. Indeed, several up-to-date experiments have adopted such methodology in their benchmark studies and presented a comparison between different sensor performances under various weather conditions [6][53][54][4]. It is noteworthy that most of the commercial LiDAR systems can directly provide signal intensity information or SNR, which reduces the computational effort in the post-processing. However, the real challenges lie on the accurate controlling of environmental parameters and the collection of data with robust statistics.

The theoretical work predicts the LiDAR extinction and backscattering coefficient under foggy conditions [55]. The assumption of spherical particle and the single scattering process of light is proved to be valid in fog by the Monte Carlo Simulation [56]. Similarly, given the single scattering assumption, the impact of rainy conditions on laser radar is also studied. Simulation work shows that the radar detection range can be reduced by 55% in extreme rainy conditions (400mm/hr) [57]. A more complex pattern is observed in an experimental study that under rain influence, the reflected points of LiDAR can be shifted closer to the emitter [4]. Additionally, it is interesting to observe that comparing to fog and rain droplets, snow particles have been less studied with commercial LiDAR systems in the literature. In fact, there is a lack of research in methods to improve LiDAR data under snow influence [58]. Although the large size of snowflakes may generate Mie scattering like fog particles and rain droplets, different laser attenuation should be expected due to its unique microphysical model and precipitation speed [55]. This work will be meaningful, especially in Minnesota, where it snows on average 110 days per year with a cover of one inch (2.5 cm) or greater [56]. Secondly, many benchmark studies of commercial LiDAR systems are strongly dependent on the Kruse model, which is derived empirically. Efforts to develop new analytical models or semi-empirical models to improve the accuracy in both assessment and prediction are necessary. Simple Monte Carlo simulations can be implemented with the new model to make comparisons with future experimental data [59].

## 1.5 CONCLUSIONS

In this chapter, applications of LiDAR techniques to fundamental research of atmospheric particles and use in autonomous vehicles have been reviewed. The former emphasizes the characterization of the aerosol microphysics and optical properties, while the latter seeks solutions to reduce particle effects on LiDAR signals. Adverse weather including fog, haze, rain and snow, not only reduces the maximum range of detection [60], but also causes the attenuation in signal intensity. To investigate and benchmark phenomenon as such, the experimental study and methodologies from literature have been discussed in sections 1.3 and 1.4, based on which some research ideas are offered as well in subsection 1.4. Experiments in the literature show a complex pattern of LiDAR signals. It is, therefore, important to reconsider assumptions such as the single scattering process in deriving new analytical models of predicting backscattering and extinction coefficients under adverse weather conditions. The literature review shows the value of this project, which not only will extend the knowledge of LiDAR applications in unfavorable weather but will also shine more light on the hardware design of LiDAR systems. In fact, as an example, Velodyne has upgraded their system by implementing a digital signal processor that can automatically switch intensity in the laser emitter according to the surrounding environment [61].

# CHAPTER 2: FOG PARTICLE EXPERIMENT

## 2.1 TEST PROCEDURE

The chamber setup is identical to the one in memorandum of Task 5, except the fog machine was replaced by a new model with higher output power, the target was covered by aluminum material. A Belfort Model 6400 visibility sensor (Grants Pass, OR) was mounted at the center of the chamber. The inner view and objects dimension are reported in Fig. 1 (a). Fig. 1 (b) shows the view of setup from the viewpoint of the LiDAR system, where the different color represents the value of an internal LiDAR parameter, Range Corrected Directional Reflectance (RCDR). This non-dimensional parameter is defined as the ratio of backscattered laser energy over the emitted energy, which describes the portion of energy received by the sensor. It is particularly of interested that how the fog particles can affect RCDR value from sensor. Meanwhile, a spatial averaging technique was used in this work to compensate for single laser beam variability in the time series data. The spatial averaging sensitivity was confirmed by taking mean of the data from different areas on the reflective object. Although the size of area where spatial averaging was implemented varied, the mean value remained approximately the same. Therefore, it is reasonable to use a spatially averaged value to represent the changes in LiDAR signal.
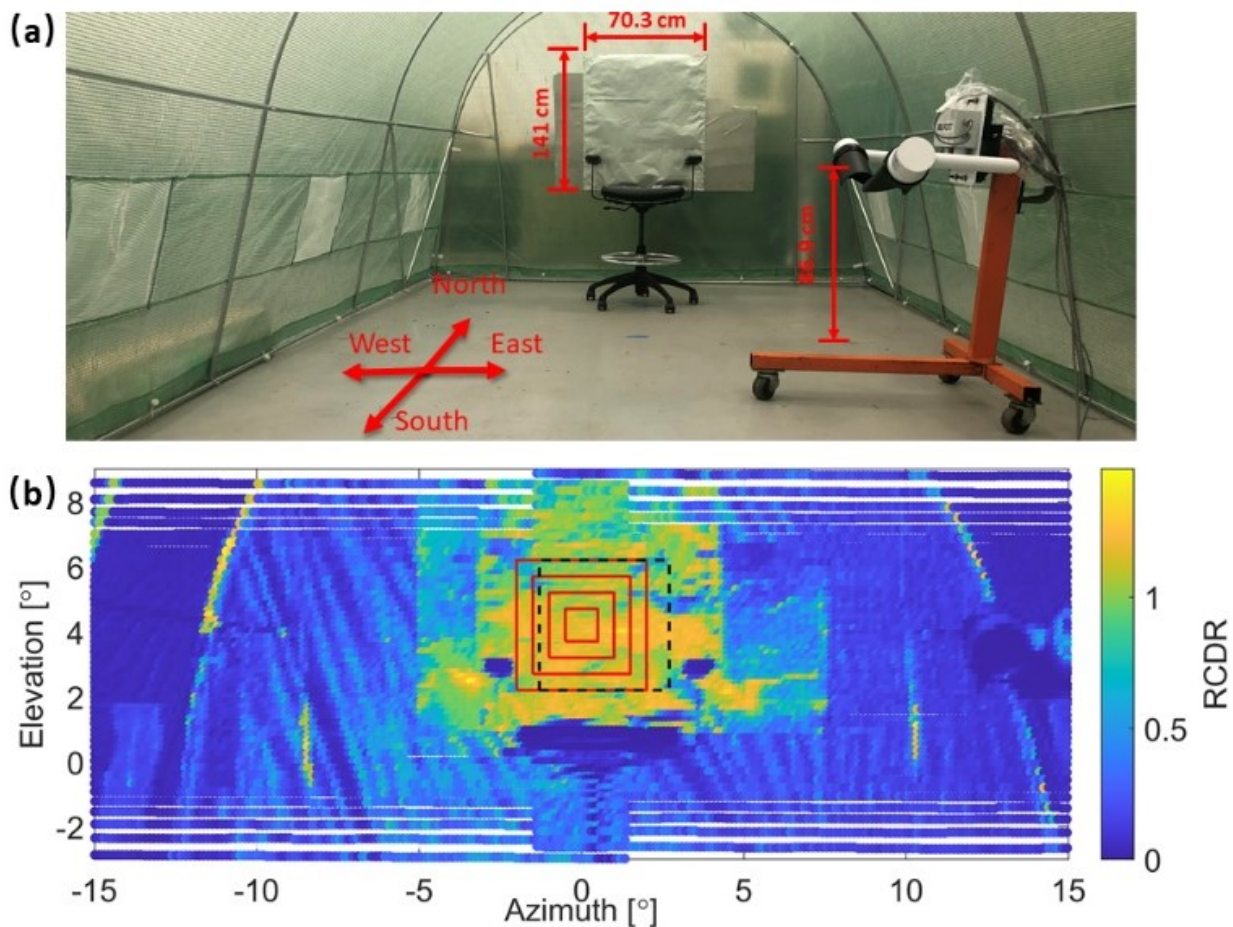


**Figure 1. (a) Experimental setup inside the chamber. The dimension of the object and the height of the visibility sensor receiver are displayed. The North direction is given by an arrow. (b) RCDR data measured by LiDAR**

Preliminary tests were carried out before filling up the chamber with fog. The vert first step was to characterize the temperature drift of the LiDAR system using the setup shown in Fig. 1. LiDAR data was recorded continuously while system temperature was monitored. The second test was to take measurements from the visibility sensor without fog. The receiver was rotated within the chamber to eight cardinal orientations and compared to data taken outside the chamber. These experiments were conducted to understand the impact of the non-fog chamber environment on the extinction coefficient measurement and establish ground-truth baseline data for the later comparison with fog experiments.

Once the visibility sensor and LiDAR instruments were characterized, fog particles were released into the chamber from the fog machine. The procedural steps of the fog experiment are summarized as follows:

1. Initial condition: Record 10 minutes of data with the current setup as a reference in the clear chamber;
2. Fog condition: Generate a fog plume with constant fog machine output power. The release process duration is 5 seconds and is repeated four times with a one-minute interval between release events;
3. Homogeneous condition: Wait for 20 minutes until the fog particles are fully mixed inside the chamber;
4. Fog diffusion: In this step, open all the roll-up windows on the chamber to ventilate the fog particles. This step takes approximately 70 minutes;
5. Exhaust fan: A 1000 W exhaust fan is placed outside of the chamber to create turbulent flow to purge all the fog particles. The chamber should recover back to its initial condition. This step takes about 20 minutes.

## 2.2 SENSOR CHARACTERIZATION

When a LiDAR system is turned on at the temperature of surrounding environment, its electrical components continuously generate heat and lead to a temperature drift observed in the recorded data. An independent test was conducted to characterize the temperature drift of LiDAR sensor used in this work. In Fig. 2, the increase in LIDAR system temperature and the corresponding changes in range measurement and Range Corrected Directional Reflectance (RCDR) are provided after instrument startup. The LiDAR data are spatial averaged for the largest red rectangular area given in Fig.1 (b). The range measurement changed from 5.113 m to 5.061 m (by 1% increments), which can be considered negligible. However, the RCDR output changed from 1.18 to 1.063 (by 13%) due to temperature drift, which then has less effect on RCDR after 17:02:24. The criteria to record data therefore is deduced to be when the difference between minimum and maximum system temperature is less than 0.1, which is achievable after an approximately one-hour warm-up time.
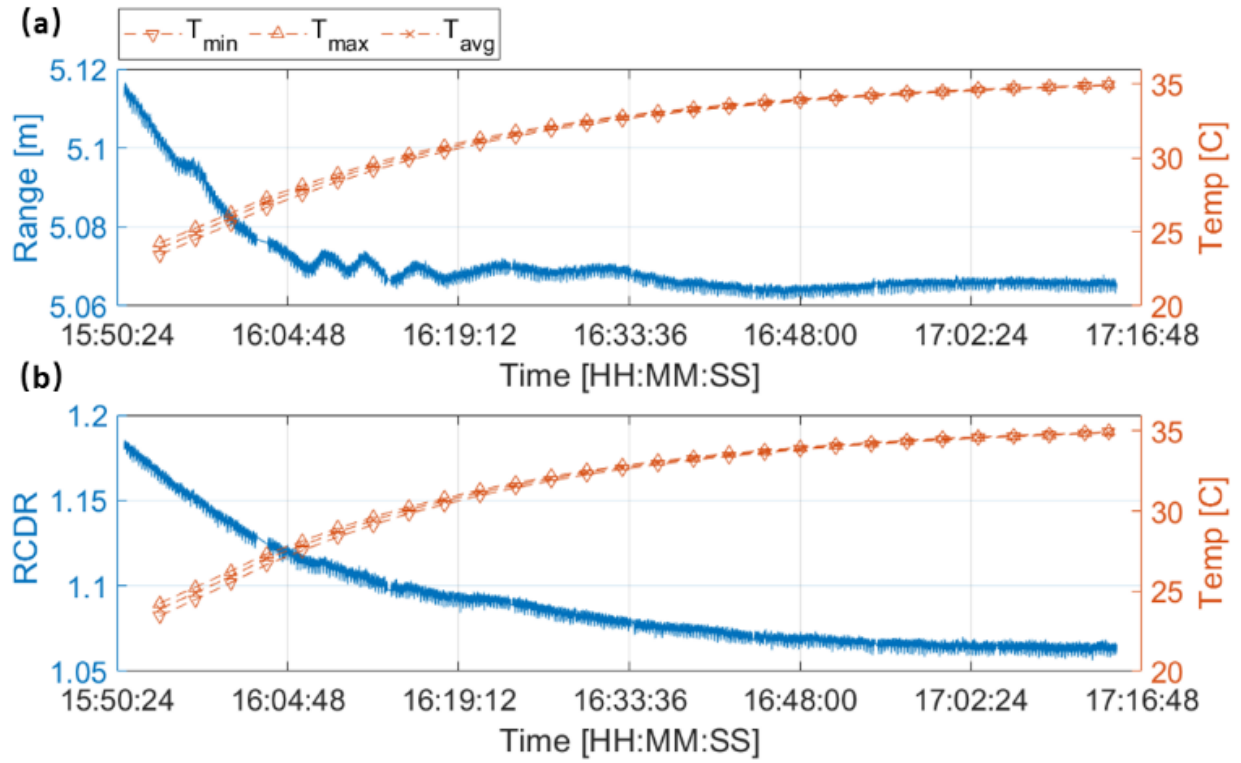
**Figure 2.** The effect of temperature drift on the (a) range measurement and (b) RCDR from the LiDAR sensor. Three values of system temperature are reported, including minimum, maximum and average for each 3-minute collection period.
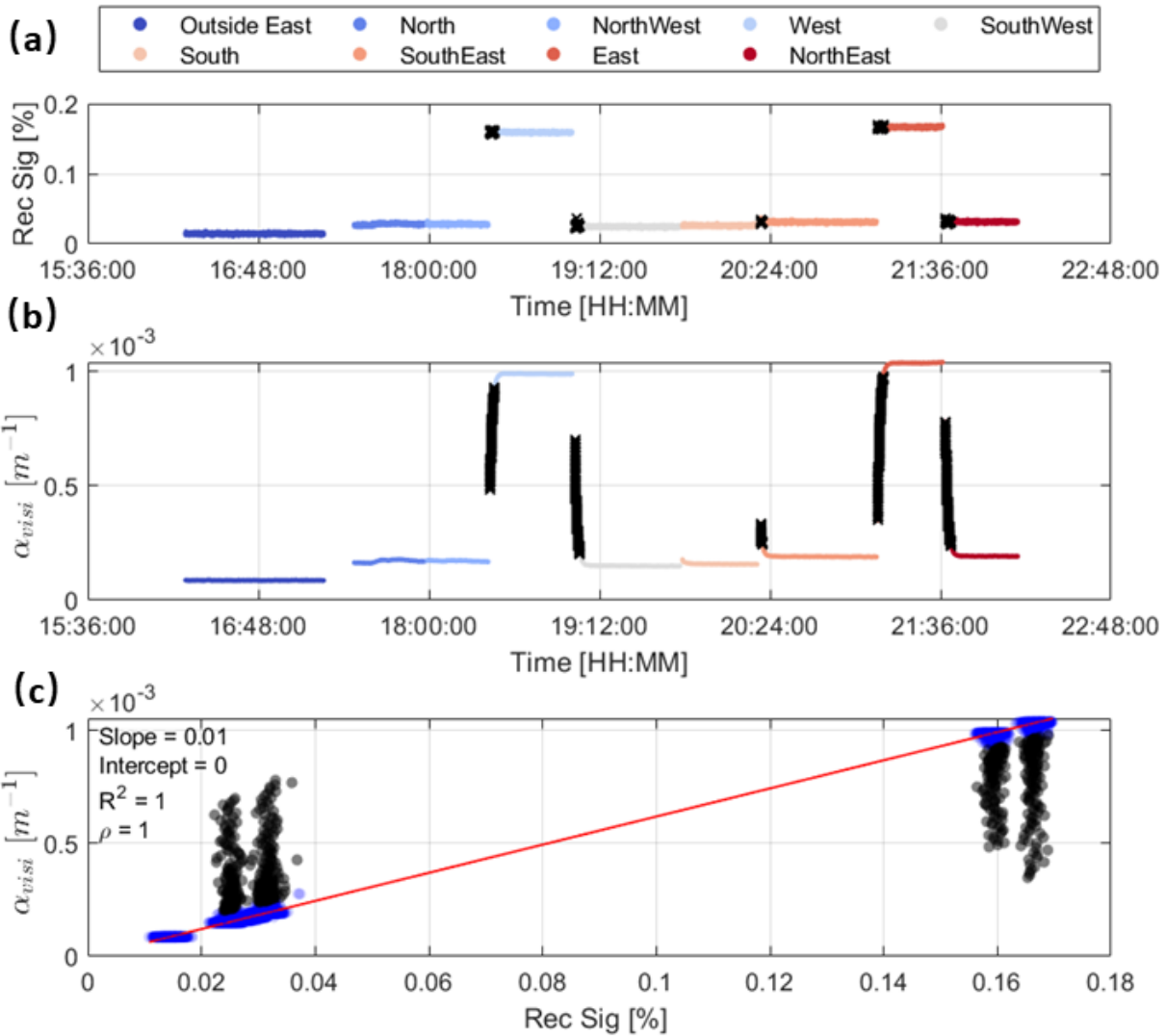
**Figure 3. The visibility sensor was oriented in eight cardinal directions and placed inside or outside the chamber. Two outputs from the sensor are plotted: (a) The percentages of Received Signal of full scale, (b) Extinction Coefficient $\alpha_{visi}$, $[m^{-1}]$. The linear correlation is plotted in (c). Black crosses in (a) and (b) are the outliers identical to the black dots in (c).**

The first visibility sensor characterization experiment was to collect a reference dataset by deploying the sensor outside the chamber with receiver pointing East (named 'Outside East' in Fig. 3). Additionally, the relation between the chamber orientation and four cardinal directions, North, South, East and West, are specified in Fig. 1(a). It is clear that the extinction coefficient measured outside the chamber had the lowest value, corresponding to longer visibility range. All orientations inside the chamber provided similar extinction values with exception to the West and East directions. By comparing the measurement inside and outside the chamber, interference with the tunnel chamber was the main reason for the increased extinction coefficient. This was especially apparent when the sensor was oriented towards East or West, where the chamber surface was in the line-of-sight of both receiver and emitter. Although the result shows that it is challenging to observe a ground-truth extinction coefficient value, the visibility

sensor was installed with Southern orientation for further experiments to minimize the impact from the chamber.

## 2.3 RESULTS AND DISCUSSION

Range measurement, RCDR and extinction coefficient are reported in Fig. 4 as a function of time according to the experimental steps described previously. In region *I*, the LiDAR reads the range of about 5.025 m and RCDR of 1.149 at the initial condition. Once the fog machine was turned on, a peak value of RCDR is observed in region *II* while the extinction coefficient increased rapidly. It is noteworthy that a constant extinction coefficient $\alpha_{visi}$ in region *III* does not reflect a stationary status of the fog particles but rather the upper limit of the visibility sensor (although not shown in figures, this has been verified by using the data quality control criteria in previous section). Surprisingly, although the RCDR measurement exhibited a chaotic evolution, the LiDAR system exhibited a very accurate measurement of the distance from the object. When the minimum visibility range measurement of 3.3 m was achieved in region *II*, the LiDAR system only overestimated the object distance by 2 cm.
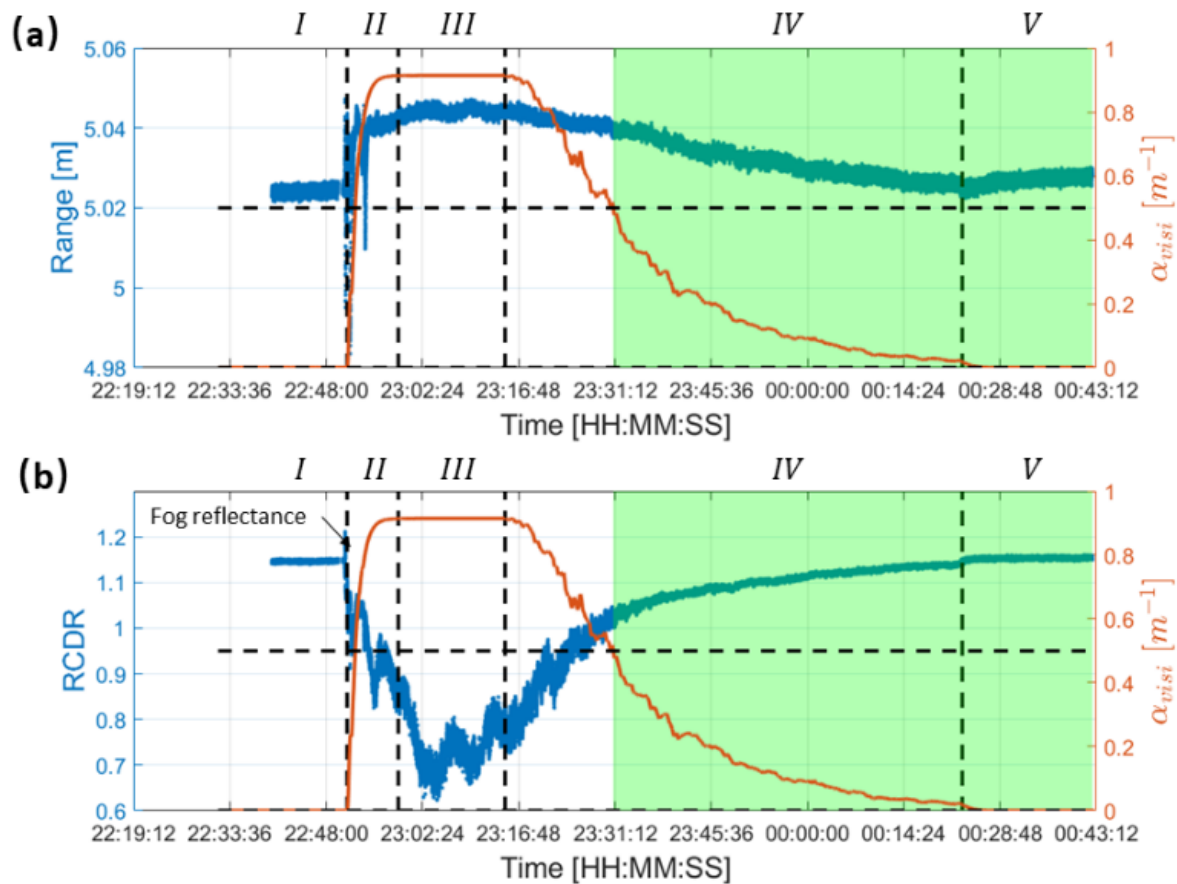
**Figure 4. Time series of (a) range measurement and (b) RCDR from LiDAR system (blue lines) and extinction coefficient $\alpha_{visi}$ from visibility sensor (Orange lines). Black vertical lines divide the experiments into five regions. The horizontal lines are the upper and lower limit of the visibility sensor capacity. The green area refers to the good dataset for modeling.**

The process in region *III* appears relatively complex as the range measurement tended towards a steady value while RCDR remained fluctuating. This may be due to many factors like changes in local fog density due to small-scale movement of fog particles or clusters, multi-scattering (defined by the phenomenon where photons were scattered multiple times before reaching back to the detector), or internal adjustment of the LiDAR sensor. However, as soon as the fog particles were vented from the chamber in region *IV*, the change in fog density dominated other factors. In Fig. 4 (a), the range measurement decreases monotonically starting at 23:14, and RCDR is increasing steadily. Meanwhile, the visibility sensor read a continuous reduction in extinction coefficient. The exhaust fan was turned on in region V at 00:23, which caused a small discontinuity in the time series of both LIDAR and visibility sensor

As seen in region *IV and V* (green area), LiDAR RCDR is strongly correlated with the extinction coefficient. To further investigate this, if constant values of extinction coefficient and backscatter coefficient are assumed, we can calculate the changes in extinction coefficient from LiDAR data by using a ratio of the RCDR measurements:

$$\Delta\alpha_{LiDAR} = \frac{\log\left(\frac{I}{I_{ref}}\right)}{-2R} \tag{1}$$

Following the comprehensive sensor characterization experiments, the $\Delta\alpha_{LiDAR}$ value is finally compared with extinction coefficient measured by visibility sensor. The result is reported in Fig. 5 (a), where a linear regression was suitable for fitting $\Delta\alpha$ from the LiDAR and the same value from the visibility sensor. The correlation coefficient from the fitting is found to be 0.98 with an r-squared of 0.97. The fitted linear model is expressed as:

$$\Delta\alpha_{LiDAR} = 0.02562 * \Delta\alpha_{Visi} - 0.01 \tag{2}$$

This result can be further extended to reveal the following expression:

$$I = I_{ref}e^{-2R(0.02562\Delta\alpha_{visi}-0.01)} \tag{3}$$

Equation (3) demonstrates an empirical approach to estimate RCDR from the LiDAR system as a function of ambient visibility for the condition of fog. The input is a reference value $I_{ref}$, the distance from an object to the LiDAR $R$ and two corresponding measurements from visibility sensor to form $\Delta\alpha_{visi}$. A comparison between the original signal and the predicted signal is reported in Fig. 5 (b). The derived model performs very well in predicting the trend of the LiDAR measurement in foggy ambient conditions. Although the linear model did not capture the high frequency variation in the original signal, the Root-Mean-Square Deviation (RMSD) between experimental data and prediction is 0.007
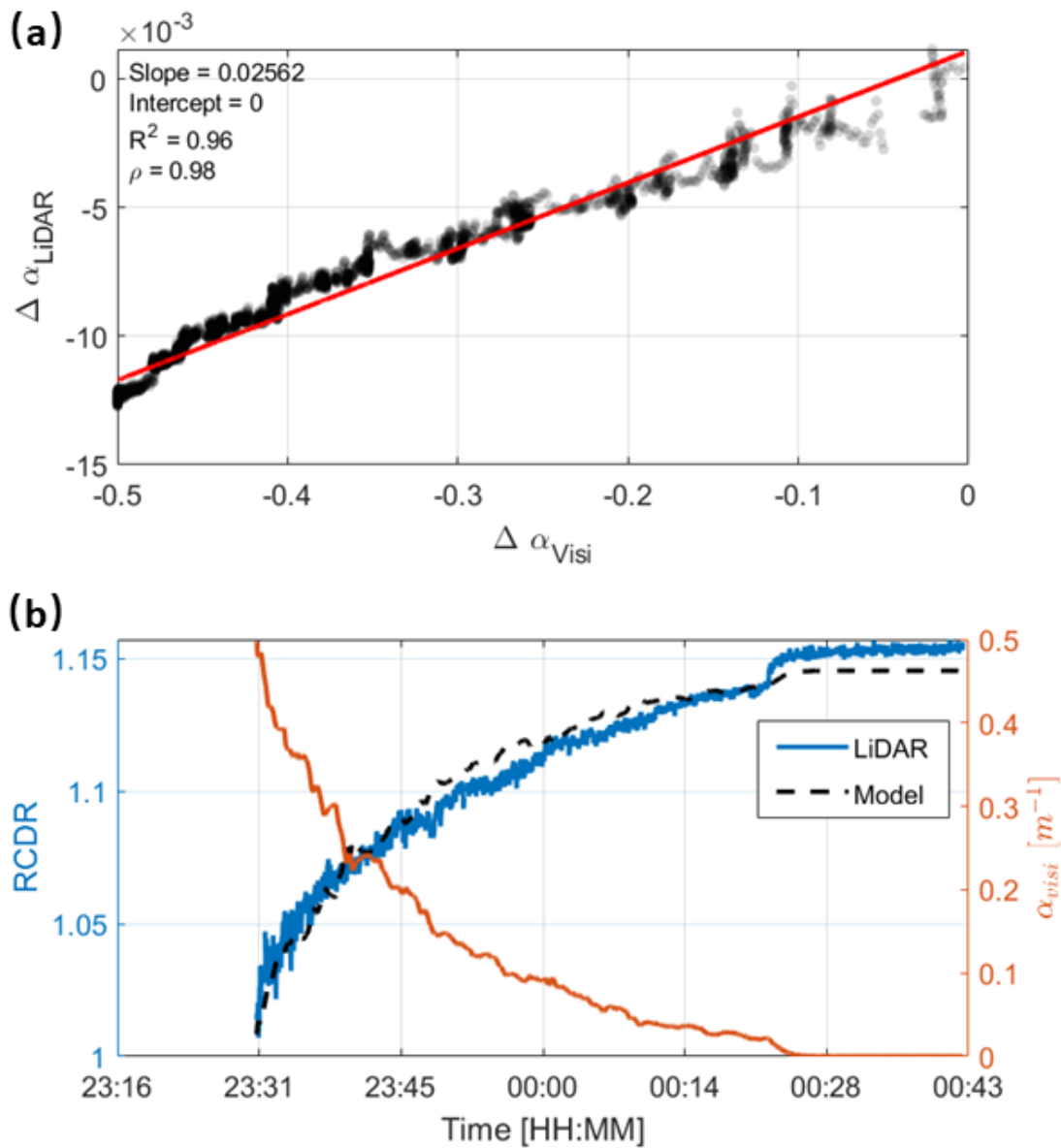
**Figure 5. (a) Linear correlation of the extinction coefficient difference measured by LiDAR and visibility sensor. (b) Time history of LiDAR RCDR in blue, and the model predicted RCDR marked by black dash line. Orange line is extinction coefficient $\alpha_{visi}$ from visibility sensor.**

## 2.4 CONCLUSIONS

In this fog chamber experiment, a prototype LiDAR sensor was correlated to extinction coefficient data provided by a visibility sensor instrument in the presence of fog inside a controlled chamber. Preliminary characterization experiments were performed to better understand the instruments and improve the

accuracy of reported results. Preliminary results demonstrated the measurement uncertainty introduced by LiDAR system temperature drift. During the fog experiments, it was found that the LiDAR system resulted in a robust and accurate measurement of the distance from an object even when the reported visibility range was lower than 6 m. Furthermore, the correlation coefficient between the RCDR measured by LiDAR and extinction coefficient from visibility sensor was found to be 0.98. The RCDR measurement was predicted in fog with a RMSD of 0.007 between the LiDAR original signal and prediction using a developed linear model. This modeling approach can be extended to different aerosol particles or testing environments in future work. The benchmark results of LiDAR RCDR in the presence of fog particles will benefit the characterization, calibration, and design of LiDAR systems to operate accurately under adverse weather conditions.

# CHAPTER 3:  SNOW PARTICLE EXPERIMENTS

## 3.1 EXPERIMENTAL DESIGN AND PREPARATION

Two types of experiments have been conducted in this section, namely road test and static test, where the former refers to the experiment with a driving vehicle, while the latter requires a stationary installation of LiDAR. To collect the LiDAR data while driving, the Luminar H3 LiDAR needs to be mounted on the roof of the vehicle. A mounting plate was prepared with 9.5 inches in width and 7.9 inches in length accordingly (a). Since the plate is made of carbon fiber, it is easy to drill 4xM4 clearance holes for platform mounting. Four M4 bolts with 0 .7mm thread and 100mm long were used for attaching the LiDAR onto the plate (b). Eventually, the LiDAR and mounting plate were installed on a 3D-printed rack that is already setup on the roof of the vehicle (c). All the power units, AD/DC converter, SSD, network router, are fixed to the rear trunk along with an additional cooling system (d). It is noteworthy that the sensor does not have inertial measurement unit (IMU) to compensate the vibrations and it follows the standards from SAE J1211. The sensor accuracy is within 1 cm for every data point and the external idle vibrations are therefore very minimal. However, if the vertical center offset is not negligible, we will consider external equipment to mitigate the vibrations.



(a)

(b)



(c)

(d)

Figure 6. (a) Measurement of the LiDAR dimension. (b) Install the LiDAR on a carbon fiber plate. (c) Mount the carbon fiber plate on the roof rack of vehicle. (d) Fit the storage and power units in the back trunk.

The first on-road experiment was designed to test the system capability and stability. Envision, a software provided by Luminar Inc, has been used to visualize the measurement in real-time. Afterwards, we used MATLAB to make customized visualization videos thru Pcap data files. VSI labs has Ouster LiDAR available during the test. The data from two systems were compared in terms of range data and signal intensity.

Compared to the stationary chamber experiment, it is reasonable to expect differences in the data from a mobile vehicle. The faster the speed of the vehicle, the less time required by the LiDAR system to measure an object. However, to select an optimal sampling frequency is not trivial since higher frequency can increase streamwise resolution for a moving object while lower frequency can improve spanwise resolution. In the next phase, we will study the resolution trade-off in different dimension and look for the best practice. In this preliminary study, we only considered two factors to explore the dynamic, namely vehicle velocity and LiDAR sample frequency. Four datasets were designed and collected with various driving speeds (miles/hour) and sampling frequencies (Hz), which are listed below:

- $1^{st}$: 5 mph and 10 Hz.
- $2^{nd}$: 10 mph and 10 Hz.
- $3^{rd}$: 20 mph and 20 Hz.

$4^{th}$: 30 mph and 20 Hz. Each dataset includes around five minute durations. The vehicle velocity refers to the maximum speed in the driving test, since we must remain at low speeds due to safety reasons, such as stop signs or speed bumps. The vehicle engine ran continuously to power the LiDAR system. Data visualizations is shown in four videos (YouTube link: https://www.youtube.com/watch?v=NKgY8IAoo5s&list=PLO2aoKkVlPh1YF6S1K_p7mRKbNL8joTHo&index=4). A virtual tour video is also shared in the same YouTube channel. A narrative below can provide more details of the vehicle operation and surrounding environments during the test.

To fully understand the influence of ambient particles on LiDAR perception, a baseline measurement was needed to document the LiDAR performance and reflectivity of objects on the road in a 'clean' environment. To design an experiment that includes as many types of objects as possible, we adopted the proposed clusters shown below [62]:

**Table 1 Proposed clusters by Behley et al., 2019**

| Cluster | SemanticKITTI Classes |
|---|---|
| Vehicle | car, bicycle, motorcycle, truck, other-vehicle, bus |
| Human | person, bicyclist, motorcyclist |
| Construction | building, fence |
| Vegetation | vegetation, trunk, terrain |
| Poles | pole, traffic sign, traffic light |
| Artifacts | sky, road, parking, sidewalk, other-ground |

The first baseline experiment took place on 02/01/2021. The baseline experiment's goal was to record most, if not all, of the objects from different classes. Therefore, the driving routine was designed to include a mix of scenarios including highway roads, neighborhood streets, and a park. It was challenging to find pedestrians outside on the road during the winter season. Luckily, some brave residents were found exercising at the park during the baseline experiment collection period.

## 3.2 CHALLENGES IN ON-ROAD EXPERIMENT

The on-road experiment was carried out on 02/17/2021 with moderate snow and 03/15/2021 with a snowstorm. Comparing with the dataset collected on a sunny day, we observed an interesting phenomenon. Between Fig.7 (a) and Fig.7 (b), without snow or water covered on the ground, the LiDAR system can detect the traffic lanes since pavement and paintings have different reflectivity in light. However, the lane markings will not be seen if covered by snow or water (melted snow due to the passing traffic). Moreover, the snow layer on the ground generally returns a signal with low reflectance. It is essential to detect the lanes and feed this information to the lateral controller while an autonomous vehicle plans a lane-changing operation or passing by a front vehicle.
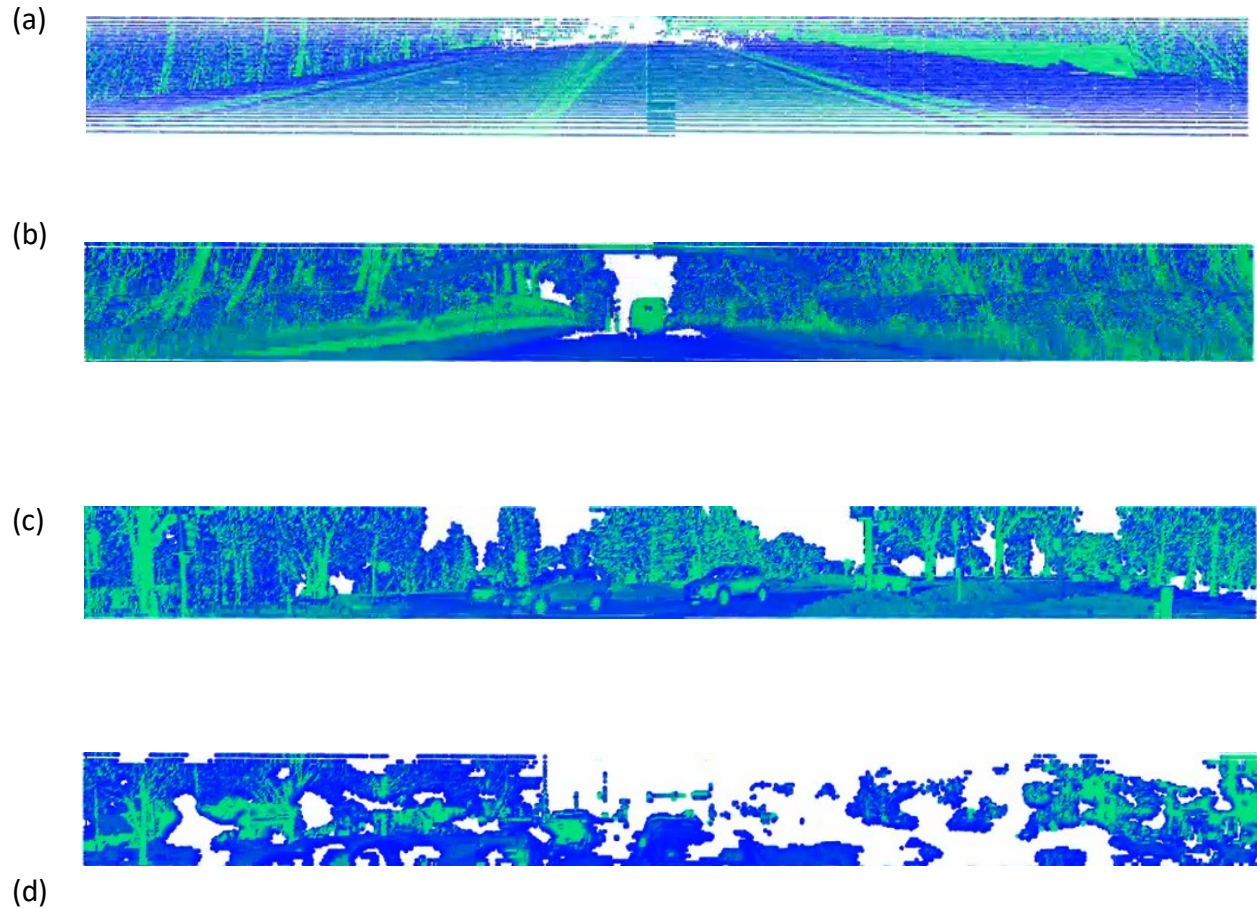
(a)



(b)



(c)





(d)

**Figure 7. Image (a), (c) below show the object reflectance measurement by LiDAR in the baseline case, while images (b), (d) are the same type of LiDAR data but recorded with moderate snowfalls.**

Fig 7. (d) shows a significant amount of white (blank) areas randomly distributed in this 2D-view dataset. The white areas are due to the snow particles on the LiDAR lens surface, which quickly transforms into an ice layer after contact, and continuously scatters and distorts the laser signal. Such circumstance largely deteriorates in the snowstorm. In the worst case, the LiDAR system will not see a single vehicle on the highway. Although Luminar H3 LiDAR is claimed to be IP67 compliant, which means the system can function under adverse conditions such as rainy, snowy, or foggy weather, the experimental data shows the LiDAR cannot 'see' through the thick ice layer.

Interestingly, the LiDAR system can see the particles and water droplets spun off from the front vehicle's rear tires. The particles presented a highly complex pattern in movement and shape. Particles and droplets experience the influence of the vehicle wake flow, which caused the meandering movement in a lateral direction. On the other hand, they intended to mix with vehicle emissions where high-temperature air will melt the snow particles instantly. Additionally, as the particles spread and diffused in a downstream direction, a lower particle density will return less signal to the LiDAR system. As a

result, the LiDAR can only see the sprays very close to the target vehicle, instead a far downstream position.

Fig. 8 (a) shows how the ice was formed on the LiDAR lens in a snowstorm. To record meaningful data, the LiDAR lens was manually cleaned every 3 minutes. This cleaning process was not feasible on the highway. There is no doubt that the ice blockage has significantly affected the LiDAR perception. It is almost impossible to record valid data without solving this challenge and ensuring safety in full automation by using a LiDAR sensor. We have reported this issue to Luminar and received feedback that this is still an unresolved issue in the system.

The suggestion based on this finding is that a hardware design needs to be refined to keep the LiDAR lens 'clean'. Although we can think of installing an auto-wiping system or redesigning the device structure, the new generation of the automated vehicles shown in Fig. 8 (b), seems to have great potential to avoid snow or ice blockage by installing the LiDAR internally. It is anticipated that if water-repellent material is used in the new design, the influence from ice accumulation will be largely reduced. However, this assumption has not been tested to date.
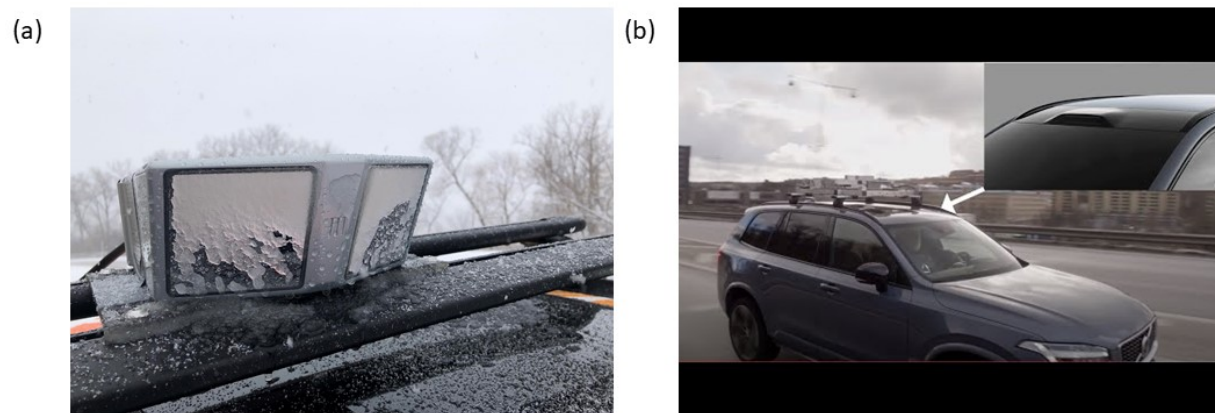


**Figure 8. (a) A thick layer of ice-covered Luminar LiDAR lens. (b) The next generation of Volvo cars powered by Luminar LiDAR, Photo credit: https://www.media.volvocars.com/**

## 3.3 STATIONARY SNOW EXPERIMENT

We conducted a static test during the snowstorm event on 03/15/2021 by installing the LiDAR indoors to avoid ice accumulation on the lens while the laser measured objects in an open area with natural snowfalls. The positions of the sensor and target are shown in Fig. 9 (a). One specific snapshot of the LiDAR reflectance data was plotted in two types of coordinates in Fig. 9 (b) and (c), where we can see some scatter points distributed randomly in space and marked by red dots that are close to the LiDAR. These scatter points are reflectance from snow particles in the air. However, unlike the fog particles, the impact from snow is not as 'continuous' as the one from fog, where a homogenous cluster is expected to scatter

the laser rays continuously. This is reasonable since fog particles has a smaller size but generally higher density than snow particles.

Furthermore, the heterogeneity of snow distribution can bring considerable uncertainty into the analysis since the sampling volume of automated LiDAR and visibility sensor is different (Volumn sampling versus point sampling). It is observed that the reflected signal from the object, the vehicle in Fig. 9 (a), is not correlated with the changes in extinction coefficient. Instead, the noise-like signal seems to vary according to the extinction coefficient in Fig. 10.
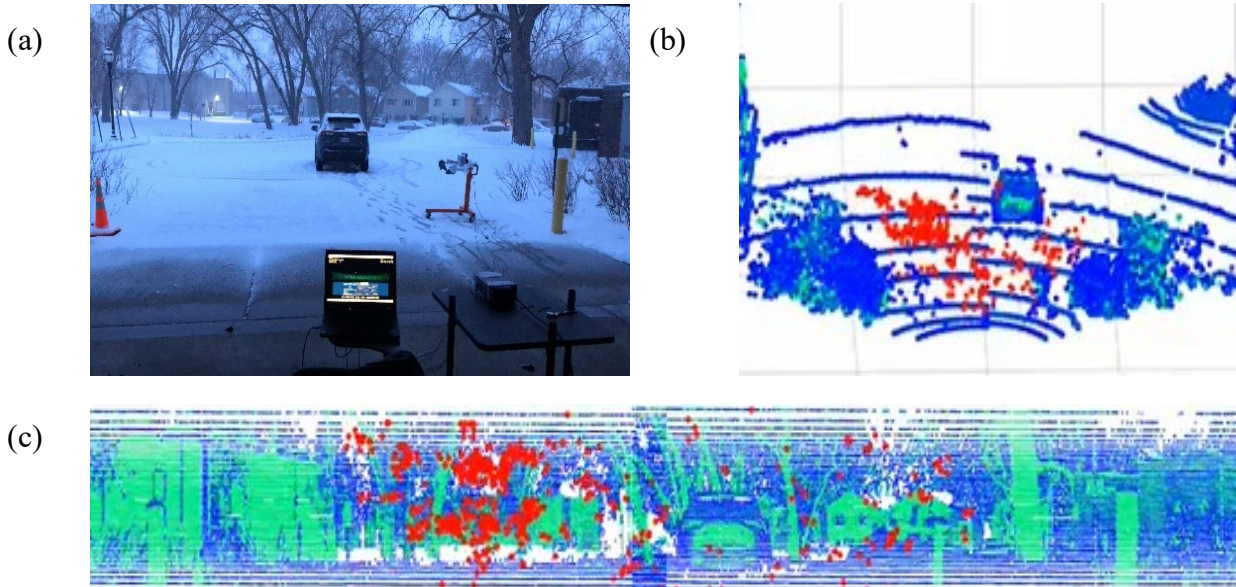


**Figure 9. (a) The experimental setup of comparison test; (b) LiDAR reflectance measurement plotted in a 3D coordinate of XYZ; (c) LiDAR reflectance measurement plotted in a 2D coordinate of azimuth and elevation angle. Red dots mark reflectance from snow particles.**
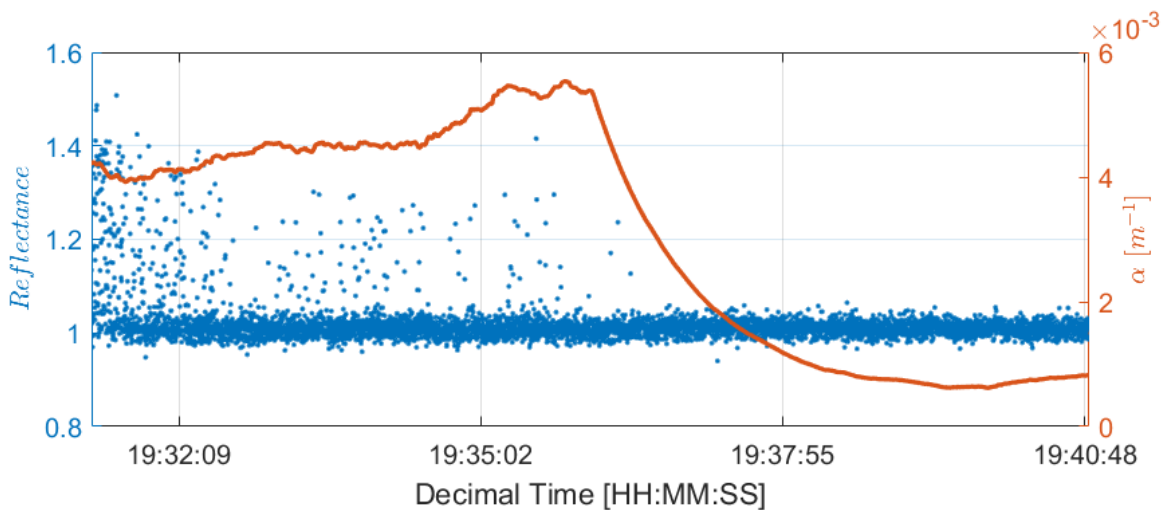


**Figure 10. Time history data of LiDAR reflectance marked by blue dots and extinction coefficient measured by visibility sensor denoted as a solid orange line.**

The histogram of the data, which is not shown here, found that the backscattered signal from snow particles generally has a very low reflectance value. To extract the snow position, a filter was applied to the snapshot. This filter can be described as:

$$f = f(r, I | I \leq I_{snow}, r < r_0, r\sin(\varphi) > z_{ground})$$

Where $I_{snow}$ is the characteristic reflectance value for snow particles, $r_0$ is the radius at which the laser signal is significantly affected, and $z_{ground}$ is a value to exclude the sampling points on the ground. The filtering effect is reported in Fig. 11.
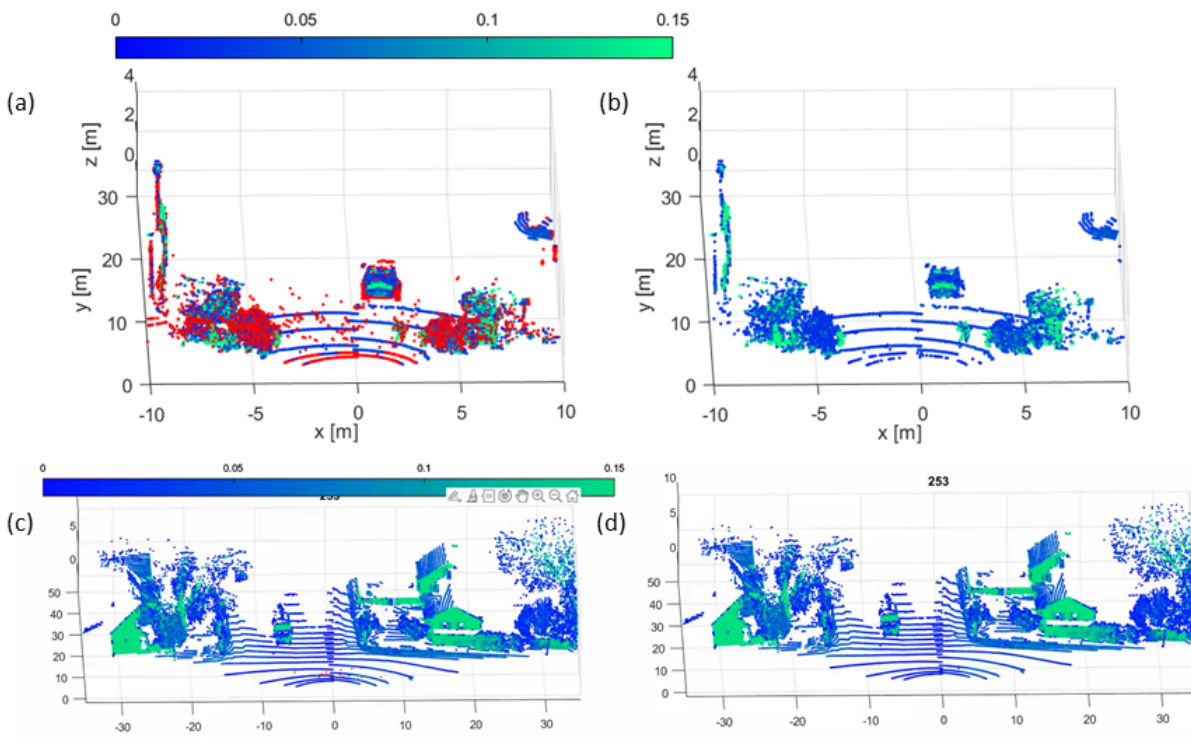


**Figure 11. (a) Stationary data before filtering; (b) Stationary data after filtering; (c) On-road data before filtering; (d) On-road data after filtering**

If the snow event is severe, more data points are filtered in Fig. 11 (a) and (b). Meanwhile, a few outliers near the LiDAR are removed during the moderate snow weather in Fig. 11 (c) and (d). This filter can be implemented to reduce complexity in the dataset before any high-level algorithms such as object detection or semantic segmentation start to play a role. Based on this result, a dynamic filter is recommended to exclude the outliers in LiDAR data due to ambient particles.

## 3.4 CONCLUSIONS

In this chapter, we summarized two experimental campaigns and presented the significant findings and corresponding analysis on the LiDAR system. The key points were:

- LiDAR data was mainly corrupted due to the ice accumulation on the LiDAR lens. Improvement will be required in hardware to palliate such blockage effects.
- A snow particle filter was designed and tested with the LiDAR data and showed the greatest potential to remove the outliers due to adverse weather. Applying such a filter can be beneficial in the data post-processing and algorithm improvement analysis.

# REFERENCES

[1] J. Hecht. (2010).  A short history of laser development. *Applied Optics*, *49*(25), F99–F122.

[2] M. E. Warren. (2019). Automotive lidar technology. In *2019 Symposium on VLSI Circuits*, C254– C255.

[3] *The Road to Full Automation by National Highway Traffic Safety Administration (NHTSA*). Retrieved from https://www.nhtsa.gov/technology-innovation/automated-vehicles-safety.

[4] S. Hasirlioglu, A. Kamann, I. Doric, & T. Brandmeier (2016). Test methodology for rain influence on automotive surround sensors. In *2016 IEEE 19th International Conference on Intelligent Transportation Systems* (ITSC), 2242–2247.

[5] W. C. Hinds. (1999). *Aerosol technology: properties, behavior, and measurement of airborne particles.* Hoboken, NJ: John Wiley & Sons.

[6] M. Bijelic, T. Gruber, & W. Ritter. (2018). A benchmark for lidar sensors in fog: Is detection breaking down? In *2018 IEEE Intelligent Vehicles Symposium (IV),* 760–767.

[7] M. Imaki & T. Kobayashi. (2005). Ultraviolet high-spectral-resolution doppler lidar for measuring wind field and aerosol optical properties. *Applied Optics*, 44(28), 6023–6030.

[8] R. C. Hardie, M. Vaidyanathan, & P. F. McManamon. (1998). Spectral band selection and classifier design for a multispectral imaging laser radar. *Optical Engineering, 37*( 3), 752-762.

[9] P. F. McManamon. (2019). Lidar technologies and systems. SPIE Press, Bellingham, WA.

[10] C. Weitkamp. (2006). *Lidar: range-resolved optical remote sensing of the atmosphere, Springer Series in Optical Sciences, 102.* Springer Science & Business, New York, NY.

[11]  Ansmann, A., Müller, D. (2005). Lidar and Atmospheric Aerosol Particles. In: Weitkamp, C. (eds) Lidar. Springer Series in Optical Sciences, vol 102. Springer, New York, NY.

[12] G. Fiocco & G. Grams. (1964). Observations of the aerosol layer at 20 km by optical radar. *Journal of the Atmospheric Sciences, 2*1(3), 323–32.

[13] P. B. Russell, P. V. Hobbs, & L. L. Stowe. (1999).  Aerosol properties and radiative effects in the United States east coast haze plume: An overview of the tropospheric aerosol radiative forcing observational experiment (TARFOX). *Journal of Geophysical Research: Atmospheres, 104*(D2), 2213– 2222.

[14] J. Redemann, R.P. Turco, K.N. Liou, P.B. Russell, R.W. Bergstrom, B. Schmid, J.M. Livingston, P.V. Hobbs, W.S. Hartley, S. Ismail, R.A. Ferrare, and E.V. Browell (2000). Retrieving the vertical structure of the effective aerosol complex index of refraction from a combination of aerosol in situ and remote sensing measurements during TARFOX. *Journal of Geophysical Research: Atmospheres*, *105*(D8), 9949– 9970.

[15] F. Raes, T. Bates, F. McGovern, & M. Van Liedekerke. (2000). The 2nd aerosol characterization experiment (ace-2): General overview and main results. *Tellus B: Chemical and Physical Meteorology, 52*(2), 111–125.

[16] V. Ramanathan, P. J. Crutzen, J. Lelieveld, A. Mitra, D. Althausen, J. Anderson, M. O. Andreae, W. Cantrell, G. Cass, C. Chung, et al. (2001). Indian ocean experiment: An integrated analysis of the climate forcing and effects of the great INDO-ASIAN haze. *Journal of Geophysical Research: Atmospheres, 106*(D22), 28371–28398.

[17] E. J. Welton, K. J. Voss, P. K. Quinn, P. J. Flatau, K. Markowicz, J. R. Campbell, J. D. Spinhirne, H. R. Gordon, & J. E. Johnson. (2002). Measurements of aerosol vertical profiles and optical properties during INDOEX 1999 using micropulse lidars. *Journal of Geophysical Research: Atmospheres, 107*(D19), INX2–18.

[18] A. Ansmann, U. Wandinger, A. Wiedensohler, & U. Leiterer. (2002). Lindenberg aerosol characterization experiment 1998 (lace 98): overview. *Journal of Geophysical Research: Atmospheres, 107*(D21), LAC 11-1-LAC 11-12.

[19] B. J. Huebert, T. Bates, P. B. Russell, G. Shi, Y. J. Kim, K. Kawamura, G. Carmichael, & T. Nakajima. (2003). An overview of ACE-ASIA: Strategies for quantifying the relationships between Asian aerosols and their climatic impacts. *Journal of Geophysical Research: Atmospheres*, *108*(D23), 8633.

[20] R. Arimoto, Y.J. Kim, Y.P. Kim, P.K. Quinn, T.S. Bates, T.L. Anderson, S. Gong, I. Uno, M. Chin, B.J. Huebert, A.D. Clarke, Y. Shinozuka, R.J. Weber, J.R. Anderson, S.A. Guazzotti, R.C. Sullivan, D.A. Sodeman, K.A. Prather, I.N. Sokolik, (2006). Characterization of Asian dust during ACE-ASIA. *Global and Planetary Change, 52,* 23–56.

[21] J. N. Porter, B. Lienert, S. Sharma, E. Lau, & K. Horton. (2003). Vertical and horizontal aerosol scattering fields over bellows beach, Oahu, during the seas experiment. *Journal of Atmospheric and Oceanic Technology, 20*(10), 1375–1387.

[22] C. Muenkel, S. Emeis, W. J. Mueller, & K. P. Schaefer. (2004). Aerosol concentration measurements with a lidar ceilometer: results of a one year measuring campaign. In *Remote Sensing of Clouds and the Atmosphere VII* (pp. 486–496). SPIE, Bellingham, WA.

[23] J. A. Reagan, M. P. McCormick, & J. D. Spinhirne. (1989). Lidar sensing of aerosols and clouds in the troposphere and stratosphere. *Proceedings of the IEEE, 77(*3), 433–448.

[24] R. Penndorf. (1957). Tables of the refractive index for standard air and the Rayleigh scattering coefficient for the spectral region between 0.2 and 20.0 µ and their application to atmospheric optics. *Josa, 7*(2), 176–182.

[25] A. T. Young. (1981). On the Rayleigh-scattering optical depth of the atmosphere. *Journal of Applied Meteorology, 20*(3), 328–330.

[26] R. Collis. (1966). Lidar: a new atmospheric probe. *Quarterly Journal of the Royal Meteorological Society, 392,* 220–230.

[27] P. B. Russell, T. J. Swissler, & M. P. McCormick. (1979). Methodology for error analysis and simulation of lidar aerosol measurements. *Applied Optics, 18*(22), 3783–3797.

[28] M. Sandford. (1967). Laser scatter measurements in the mesosphere and above. *Journal of Atmospheric and Terrestrial Physics, 29*(12), 1657–1662.

[29] P. Hamilton. (1969). Lidar measurement of backscatter and attenuation of atmospheric aerosol. *Atmospheric Environment, 3*(2), 221–223.

[30] F. G. Fernald, B. M. Herman, & J. A. Reagan. (1972). Determination of aerosol height distributions by lidar. *Journal of Applied Meteorology, 11*(3), 482–489.

[31] J. D. Klett. (1981). Stable analytical inversion solution for processing lidar returns. *Applied Optics, 20*(2), 211– 220.

[32] J. Spinhirne, J. A. Reagan, & B. Herman. (1980). Vertical distribution of aerosol extinction cross section and inference of aerosol imaginary index in the troposphere by lidar technique. *Journal of Applied Meteorology, 19*(4), 426–438.

[33] R. Ferrare, S. Melfi, D. Whiteman, & K. Evans. (1992). Raman lidar measurements of pinatubo aerosols over southeastern Kansas during November-December 1991. *Geophysical Research Letters, 19*(15), 1599–1602.

[34] M. Hebert & E. Krotkov. (1992). 3d measurements from imaging laser radars: how good are they? *Image and Vision Computing, 10*(3), 170–178.

[35] J. Pascoal, L. Marques, & A. T. de Almeida. (2008). Assessment of laser range finders in risky environments. In *2008 IEEE/RSJ International Conference on Intelligent Robots and Systems*, 3533–3538.

[36] U. Wong, A. Morris, C. Lea, J. Lee, C. Whittaker, B. Garney, & R. Whittaker. (2011). Comparative evaluation of range sensing technologies for underground void modeling. In *2011 IEEE/RSJ International Conference on Intelligent Robots and Systems*, 3816–3823.

[37] E. Trickey, P. Church, & X. Cao. (2013). Characterization of the opal obscurant penetrating lidar in various degraded visual environments. In *Degraded Visual Environments: Enhanced, Synthetic, and External Vision Solutions, 8737*, 87370E.

[38] T. Peynot, J. Underwood, & S. Scheding. (2009). Towards reliable perception for unmanned ground vehicles in challenging conditions. In *2009 IEEE/RSJ International Conference on Intelligent Robots and Systems,* 1170– 1176.

[39] R. H. Rasshofer, M. Spies, & H. Spies. (2011). Influences of weather phenomena on automotive laser radar systems. *Advances in Radio Science: ARS, 9*, 49.

[40] S. Hasirlioglu, A. Riener, W. Huber, & P. Wintersberger. (2017). Effects of exhaust gases on laser scanner data quality at low ambient temperatures. In *2017 IEEE Intelligent Vehicles Symposium (IV),* 1708–1713.

[41] M. Kutila, P. Pyykonen, W. Ritter, O. Sawade, & B. Schaufele. (2016). Automotive lidar sensor development scenarios for harsh weather conditions. In 2016 IEEE 19th International Conference on Intelligent Transportation Systems (ITSC), 265–270, IEEE.

[42] M. Ijaz, Z. Ghassemlooy, H. Le Minh, S. Rajbhandari, & J. Perez. (2012). Analysis of fog and smoke attenuation in a free space optical communication link under controlled laboratory conditions. In *2012 International Workshop on Optical Wireless Communications (IWOW)*, 1–3.

[43] M. Ijaz, Z. Ghassemlooy, J. Pesek, O. Fiser, H. Le Minh, & E. Bentley. (2013). Modeling of fog and smoke attenuation in free space optical communications link under controlled laboratory conditions. *Journal of Lightwave Technology, 31*(11), 1720–1726.

[44] J. Wojtanowski, M. Zygmunt, M. Kaszczuk, Z. Mierczyk, & M. Muzal. (2014). Comparison of 905 nm and 1550 nm semiconductor laser rangefinders' performance deterioration due to adverse environmental conditions. *OptoElectronics Review, 22*(3), 183–190.

[45] M. Colomb, K. Hirech, P. Andre, J. Boreux, P. Lacote, & J. Dufour. (2008). An innovative artificial fog production device improved in the European project "fog." *Atmospheric Research, 87*( 3-4), 242–251.

[46] P. W. Kruse, L. D. McGlauchlin, & R. B. McQuistan. (1962). *Elements of infrared technology: Generation, transmission and detection.* New York: John Wiley and Sons.

[47] I. I. Kim, B. McArthur, & E. J. Korevaar. (2001). Comparison of laser beam propagation at 785 nm and 1550 nm in fog and haze for optical wireless communications. In *Optical Wireless Communications III, 4214,* 26–37.

[48] M. C. Al Naboulsi, H. Sizun, & F. de Fornel. (2004). Fog attenuation prediction for optical and infrared waves. *Optical Engineering, 43*(2), 319–330.

[49] M. Ijaz, Z. Ghassemlooy, S. Rajbhandari, H. Le Minh, J. Perez, & A. Gholami. (2012). Comparison of 830 nm and 1550 nm based free space optical communications link under controlled fog conditions. In *2012 8th International Symposium on Communication Systems, Networks & Digital Signal Processing (CSNDSP),* 1–5

[50] F. Nadeem, T. Javornik, E. Leitgeb, V. Kvicera, & G. Kandus. (2010). Continental fog attenuation empirical relationship from measured visibility data. *Radioengineering, 19*(4), 596– 600.

[51] M. Gebhart, E. Leitgeb, M. Al Naboulsi, H. Sizun, &F. de Fornel. (2005). Measurements of light attenuation at different wavelengths in dense fog conditions for FSO applications. *Proc. SPIE*, 5891, Atmospheric Optical Modeling, Measurement, and Simulation, 58910K.

[52] L. Mustafa, E. Cerncic, & B. Thomsen. (2016). Fso artificial low-cost fog attenuation experiment design. In *2016 10th International Symposium on Communication Systems, Networks and Digital Signal Processing (CSNDSP),* 1–5.

[53] M. Bijelic, T. Gruber, & W. Ritter. (2018). Benchmarking image sensors under adverse weather conditions for autonomous driving. In *2018 IEEE Intelligent Vehicles Symposium (IV),* 1773– 1779.

[54] Y. Li, P. Duthon, M. Colomb, & J. Ibanez-Guzman. (2020). What happens for a ToF lidar in fog. arXiv preprint arXiv:2003.06660.

[55] R. Nebuloni & C. Capsoni. (2008). Laser attenuation by falling snow. In *2008 6th International Symposium on Communication Systems. Networks and Digital Signal Processing*, 265–269.

[56] M. W. Seeley. (2015). *Minnesota weather almanac: Completely updated for the new normals*. St. Paul, MN: Minnesota Historical Society Press.

[57] S. Zang, M. Ding, D. Smith, P. Tyler, T. Rakotoarivelo, & M. A. Kaafar. (2019). The impact of adverse weather conditions on autonomous vehicles: how rain, snow, fog, and hail affect the performance of a self-driving car. *IEEE Vehicular Technology Magazine, 14*(2), 103–111.

[58] N. Charron, S. Phillips, & S. L. Waslander. (2018). De-noising of lidar point clouds corrupted bysnowfall. In *2018 15th Conference on Computer and Robot Vision (CRV),* 254–261.

[59] F. Taillade, E. Belin, & E. Dumont. (2008). An analytical model for backscattered luminance in fog: comparisons with monte carlo computations and experimental results. *Measurement Science and Technology, 19*(5), 055302.

[60] M.-C. Areann, T. Bosch, M. Lescure, A. R. Myllylae, & M. Rioux. (2001). Laser ranging: a critical review of usual techniques for distance measurement. *Opt. Eng, 40*(1), .

[61] D. S. Hall (2011). High definition lidar system, US Patent 7,969,558.

[62] Behley, J., Garbade, M., Milioto, A., Quenzel, J., Behnke, S., Stachniss, C., & Gall, J. (2019). Semantickitti: A dataset for semantic scene understanding of lidar sequences. In *Proceedings of the IEEE/CVF International Conference on Computer Vision*, 9297-9.